Dual-detection confocal fluorescence microscopy: fluorescence axial imaging without axial scanning

Dong-Ryoung Lee,[1] Young-Duk Kim,[1] Dae-Gab Gweon,[1,3] and Hongki Yoo,[2,*]

[1]Nano Opto-Mechatronics Laboratory, Department of Mechanical Engineering, Korea Advanced Institute of Science and Technology (KAIST), 291 Daehak-ro, Yuseong-gu, Daejeon, 305-701, South Korea
[2] Biomedical Optics and Photomedicine Laboratory, Department of Biomedical Engineering, Hanyang University, 222 Wangsimni-ro, Seongdong-gu, Seoul, 133-791, South Korea
[3]gweondg@kaist.ac.kr
[*]hyoo@hanyang.ac.kr

Abstract: We propose a new method for high-speed, three-dimensional (3-D) fluorescence imaging, which we refer to as dual-detection confocal fluorescence microscopy (DDCFM). In contrast to conventional beam-scanning confocal fluorescence microscopy, where the focal spot must be scanned either optically or mechanically over a sample volume to reconstruct a 3-D image, DDCFM can obtain the depth of a fluorescent emitter without depth scanning. DDCFM comprises two photodetectors, each with a pinhole of different size, in the confocal detection system. Axial information on fluorescent emitters can be measured by the axial response curve through the ratio of intensity signals. DDCFM can rapidly acquire a 3-D fluorescent image from a single two-dimensional scan with less phototoxicity and photobleaching than confocal fluorescence microscopy because no mechanical depth scans are needed. We demonstrated the feasibility of the proposed method by phantom studies.

©2013 Optical Society of America

OCIS codes: (180.1790) Confocal microscopy; (180.2520) Fluorescence microscopy; (180.6900) Three-dimensional microscopy; (120.3930) Metrological instrumentation.

References and links

1. R. S. Fischer, Y. Wu, P. Kanchanawong, H. Shroff, and C. M. Waterman, "Microscopy in 3D: a biologist's toolbox," Trends Cell Biol. **21**(12), 682–691 (2011).
2. E. A. Te Velde, T. Veerman, V. Subramaniam, and T. Ruers, "The use of fluorescent dyes and probes in surgical oncology," Eur. J. Surg. Oncol. **36**(1), 6–15 (2010).
3. R. Weissleder and V. Ntziachristos, "Shedding light onto live molecular targets," Nat. Med. **9**(1), 123–128 (2003).
4. D. Li, W. Zheng, and J. Y. Qu, "Two-photon autofluorescence microscopy of multicolor excitation," Opt. Lett. **34**(2), 202–204 (2009).
5. Y. Hiraoka, J. R. Swedlow, M. R. Paddy, D. A. Agard, and J. W. Sedat, "Three-dimensional multiple-wavelength fluorescence microscopy for the structural analysis of biological phenomena," Semin. Cell Biol. **2**(3), 153–165 (1991).
6. P. Prabhat, S. Ram, E. S. Ward, and R. J. Ober, "Simultaneous imaging of different focal planes in fluorescence microscopy for the study of cellular dynamics in three dimensions," IEEE Trans. Nanobioscience **3**(4), 237–242 (2004).
7. M. Gu, *Principles of Three-dimensional Imaging in Confocal Microscopes* (World Scientific, 1996).
8. J. B. Pawley, *Handbook of Biological Confocal Microscopy* (Springer, 1995).
9. R. A. Hoebe, C. H. Van Oven, T. W. Gadella, Jr., P. B. Dhonukshe, C. J. Van Noorden, and E. M. Manders, "Controlled light-exposure microscopy reduces photobleaching and phototoxicity in fluorescence live-cell imaging," Nat. Biotechnol. **25**(2), 249–253 (2007).
10. R. Dixit and R. Cyr, "Cell damage and reactive oxygen species production induced by fluorescence microscopy: effect on mitosis and guidelines for non-invasive fluorescence microscopy," Plant J. **36**(2), 280–290 (2003).
11. L. Song, C. A. Varma, J. W. Verhoeven, and H. J. Tanke, "Influence of the triplet excited state on the photobleaching kinetics of fluorescein in microscopy," Biophys. J. **70**(6), 2959–2968 (1996).
12. J. Huisken and D. Y. Stainier, "Selective plane illumination microscopy techniques in developmental biology," Development **136**(12), 1963–1975 (2009).

#190510 - $15.00 USD   Received 14 May 2013; revised 12 Jul 2013; accepted 14 Jul 2013; published 18 Jul 2013
(C) 2013 OSA   29 July 2013 | Vol. 21, No. 15 | DOI:10.1364/OE.21.017839 | OPTICS EXPRESS 17839

13. T. A. Planchon, L. Gao, D. E. Milkie, M. W. Davidson, J. A. Galbraith, C. G. Galbraith, and E. Betzig, "Rapid three-dimensional isotropic imaging of living cells using Bessel beam plane illumination," Nat. Methods **8**(5), 417–423 (2011).
14. S. Abrahamsson, J. Chen, B. Hajj, S. Stallinga, A. Y. Katsov, J. Wisniewski, G. Mizuguchi, P. Soule, F. Mueller, C. Dugast Darzacq, X. Darzacq, C. Wu, C. I. Bargmann, D. A. Agard, M. Dahan, and M. G. Gustafsson, "Fast multicolor 3D imaging using aberration-corrected multifocus microscopy," Nat. Methods **10**(1), 60–63 (2012).
15. A. K. Ruprecht, T. F. Wiesendanger, and H. J. Tiziani, "Chromatic confocal microscopy with a finite pinhole size," Opt. Lett. **29**(18), 2130–2132 (2004).
16. H. J. Tiziani and H. M. Uhde, "Three-dimensional image sensing by chromatic confocal microscopy," Appl. Opt. **33**(10), 1838–1843 (1994).
17. S. Cha, P. C. Lin, L. Zhu, P. C. Sun, and Y. Fainman, "Nontranslational three-dimensional profilometry by chromatic confocal microscopy with dynamically configurable micromirror scanning," Appl. Opt. **39**(16), 2605–2613 (2000).
18. T. Kim, S. H. Kim, D. Do, H. Yoo, and D. Gweon, "Chromatic confocal microscopy with a novel wavelength detection method using transmittance," Opt. Express **21**(5), 6286–6294 (2013).
19. K. B. Shi, P. Li, S. Z. Yin, and Z. W. Liu, "Chromatic confocal microscopy using supercontinuum light," Opt. Express **12**(10), 2096–2101 (2004).
20. Q. Xu, K. Shi, S. Yin, and Z. Liu, "Chromatic two-photon excitation fluorescence imaging," J. Microsc. **235**(1), 79–83 (2009).
21. C. A. Yang, K. B. Shi, H. F. Li, Q. A. Xu, V. Gopalan, and Z. W. Liu, "Chromatic second harmonic imaging," Opt. Express **18**(23), 23837–23843 (2010).
22. C. J. R. Sheppard and C. J. Cogswell, "Confocal microscopy with detector arrays," J. Mod. Opt. **37**(2), 267–279 (1990).
23. C. H. Lee and J. P. Wang, "Noninterferometric differential confocal microscopy with 2-nm depth resolution," Opt. Commun. **135**(4-6), 233–237 (1997).
24. W. Q. Zhao, J. B. Tan, and L. R. Qiu, "Bipolar absolute differential confocal approach to higher spatial resolution," Opt. Express **12**(21), 5013–5021 (2004).
25. J. B. Tan, J. Liu, and Y. H. Wang, "Differential confocal microscopy with a wide measuring range based on polychromatic illumination," Meas. Sci. Technol. **21**(5), 054013 (2010).
26. Y. Wang, L. R. Qiu, Y. X. Song, and W. Q. Zhao, "Laser differential confocal lens thickness measurement," Meas. Sci. Technol. **23**(5), 055204 (2012).
27. W. Q. Zhao, C. Liu, and L. R. Qiu, "Laser divided-aperture differential confocal sensing technology with improved axial resolution," Opt. Express **20**(23), 25979–25989 (2012).
28. L. M. Zou, J. Q. Qu, S. L. Hou, and X. M. Ding, "Differential confocal technology based on radial birefringent pupil filtering principle," Opt. Commun. **285**(8), 2022–2027 (2012).
29. A. Bilenca, A. Ozcan, B. Bouma, and G. Tearney, "Fluorescence coherence tomography," Opt. Express **14**(16), 7134–7143 (2006).
30. M. de Groot, C. L. Evans, and J. F. de Boer, "Self-interference fluorescence microscopy: three dimensional fluorescence imaging without depth scanning," Opt. Express **20**(14), 15253–15262 (2012).
31. T. Wilson and A. R. Carlini, "Size of the detector in confocal imaging systems," Opt. Lett. **12**(4), 227–229 (1987).
32. M. Gu and C. J. R. Sheppard, "Confocal fluorescent microscopy with a finite-sized circular detector," J. Opt. Soc. Am. A **9**(1), 151–153 (1992).
33. J. W. Goodman, *Introduction to Fourier Optics* (Roberts & Company, 2005).

1. Introduction

Fluorescence microscopy has become an essential tool in biology and biomedicine by visualizing certain molecules and cells in high contrast with endogenous and exogenous fluorescent molecules. Fluorescent imaging is used in many biological and medical applications, including analysis of cell microstructures, localization of protein expression, and measurement of dynamic molecular processes [1–6].

Confocal fluorescence microscopy has the ability to acquire optically-sectioned images from a thick specimen using a confocal pinhole to effectively eliminate out-of-focus noise [7, 8]. One of the main advantages of confocal fluorescence microscopy over conventional fluorescence microscopy is that live specimens can be observed with high resolution and contrast. In addition, confocal fluorescence microscopy can reconstruct a three-dimensional (3-D) image of a biological sample [1]. Since confocal fluorescence microscopy acquires a point image of a conjugate point with a pinhole placed in front of a detector, the point must be scanned over the specimen volume to create a 3-D image [7]. Creating a 3-D image by reconstructing a stack of 2-D images is time intensive and induces phototoxicity and photobleaching due to the repeated light exposure [9–11].

To overcome these limitations, fast 3-D imaging methods have been developed. Selective plane illumination microscopy uses light sheet illumination from the side of the sample to

create an optically-sectioned fluorescent image [12, 13]. This technique allows fast 3-D imaging with reduced photobleaching, but it suffers from spatial constraints due to the side illumination. Abrahamsson *et al.* [14] proposed multifocus microscopy, which acquires multiple images from different focal planes using specially designed gratings. However, the detection system is relatively complex, and the number of focal planes is fixed.

Three-dimensional fluorescence imaging without depth scanning is another approach to rapidly acquire three-dimensional fluorescent information and to reduce phototoxicity and photobleaching. Chromatic confocal microscopy uses a broadband light source and an objective with longitudinal chromatic aberrations, which generate multiple, axially-distributed foci depending on wavelength [15–17]. Chromatic confocal microscopy has been most widely developed using reflectance imaging for surface profiling, while several studies have investigated fluorescence and nonlinear optical imaging [18–21]. Differential confocal microscopy, which uses two or more detectors, is another method to measure surface shape with 2-D scans [22–28]. To our knowledge, fluorescence differential confocal microscopy has not yet been reported. By analyzing fluorescence self-interference signal, the location of the fluorescence signal can be determined [29, 30]. Depth discrimination technique of a fluorescent signal without a mechanical depth scan enables rapid visualization of 3-D distribution of fluorescence labels. This technique also has potential to be developed as a miniature endoscopic probe for in vivo volumetric imaging. In this paper, we propose a novel method for axial imaging without axial scanning, called dual-detection confocal fluorescence microscopy (DDCFM).
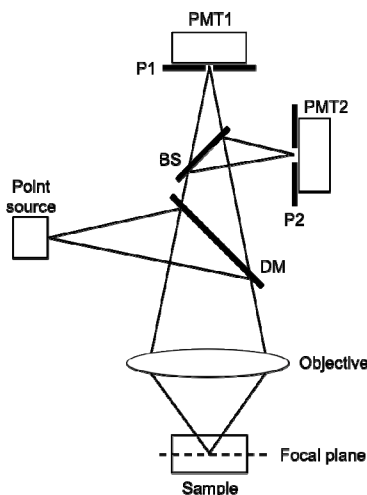

Fig. 1. Schematic of DDCFM. Light from a point source is reflected by a dichroic mirror (DM) and illuminates the sample. Light from a fluorescent emitter within the focal volume in the sample passes through the DM and is split by a beam splitter (BS). Each beam is directed to the photomultiplier tube (PMT) through a pinhole. Pinhole 1 (P1) is smaller than pinhole 2 (P2).

2. Principle of DDCFM

Figure 1 shows a schematic diagram of DDCFM, which uses two pinhole detectors with different sizes, while conventional confocal fluorescence microscopy uses only one pinhole detector. For DDCFM, light from the fluorescent sample is split by a beam splitter, then directed to two pinhole detectors. Since each pinhole is of a different size, each detector has a different axial response. Thus, a new axial response curve of the intensity ratio can be calculated from the ratio of signals received at each detector. The axial response curve of the intensity ratio indicates the relationship between the axial position of the fluorescent sample and the intensity ratio. In DDCFM, the axial distance of the sample from the focal plane can

be calculated using the intensity ratio of the fluorescent emitter. As a result, the DDCFM can be used to rapidly determine the depth of a fluorescent signal in a sample without the need for depth scanning.

The axial response curve in confocal fluorescence microscopy depends on the pinhole size. Since an out-of-focus beam is filtered by the pinhole, a detector placed behind the pinhole receives the highest signal when the fluorescent emitter is in the focal plane of the objective. In other words, the peak of the axial response curve is on the focal point, and the signal value gradually decreases as the object moves away from the focal point [31]. When light passes through the optical system, the amplitude and phase change of the field are explained as diffraction properties and are used to create the axial response curve [7]. To express the axial response curve of confocal fluorescence microscopy according to the pinhole size, the intensity of a point object with a finite-size circular detector is obtained as [7, 31, 32]

$$h_i(u,v) = |h(u,v)|^2 \left[|h(u,v)|^2 \otimes D(v) \right], \tag{1}$$

where $\otimes$ is the 2-D convolution operation, $D(v)$ is the intensity sensitivity of the detector, and $h(u,v)$ is the point-spread function (PSF) of the lens, given by

$$h(u,v) = \int_0^1 P(\rho) \exp(-iu\rho^2 / 2) J_0(v\rho)\rho \, d\rho, \tag{2}$$

where $P(\rho)$ is the pupil function of the lens, and u and v are optical coordinates defined respectively by

$$\begin{cases} v = \dfrac{2\pi}{\lambda} r \sin\alpha \\ u = \dfrac{2\pi}{\lambda} z \sin^2\alpha, \end{cases} \tag{3}$$

where $\sin\alpha$ is the numerical aperture (NA), and r and z are the radial and axial coordinates, respectively.

The PSF describes the impulse response, which is explained by Fresnel diffraction of the imaging system [33]. The intensity on the detector is determined by the square of the PSF because the intensity is the square of the field amplitude [7].

If we assume that $P(\rho)$ is a circular, uniform aperture with the same radius as the objective lens, and $D(v)$ is a circular pinhole detector [7, 31], from Eq. (1), the axial response curve becomes,

$$I(u) = \int_0^{v_p} \left| \int_0^1 \exp(iu\rho^2) J_0(v\rho)\rho \, d\rho \right|^2 dv, \tag{4}$$

where v_p represents the radius of the pinhole. As in Eq. (4), the axial response curve is a function of the axial optical coordinate, u, and the radius of the pinhole, v_p. The pinhole size determines the axial response curve, and, in general, larger pinholes generate wider axial response curves.

The fluorescence intensity is also proportional to quantum yield, which is the number of photons emitted per photons absorbed. The quantum yield varies according to the surroundings. If we account for the fluorescence quantum yield, the fluorescence intensity can be expanded as

$$I(\Phi, z) = \Phi \times I(z), \tag{5}$$

where Φ is the quantum yield, and $I(z)$ is another expression of Eq. (4) with z and a given v_p.

Since DDCFM has two detectors with different pinhole sizes, two axial response curves are generated with different full widths at half maximum (FWHM). We can calculate the intensity ratio with the small and large pinholes. Since, both intensity values are proportional to the same quantum yield, the axial response curve of the intensity ratio is independent of the quantum yield. When the two pinhole sizes are pre-determined and fixed, the intensity ratio is a function of z, yielding the following expression

$$I_R(z) = \frac{\Phi \times I_1(z)}{\Phi \times I_2(z)} = \frac{I_1(z)}{I_2(z)}, \qquad (6)$$

where $I_1(z)$ and $I_2(z)$ are the intensities detected by pinhole 1 and pinhole 2, respectively, at a specific axial position, z. The intensity ratio according to axial position becomes the axial response curve of the DDCFM system, as shown in Fig. 2. The axial position of the fluorescence emitter corresponds to a unique intensity ratio, and an intensity ratio corresponds to a unique axial position. Thus, using the axial response curves of the intensity ratio in DDCFM, the axial positions of fluorescent particles can be measured without axial scanning, even when the quantum yield of the fluorescent sample varies.
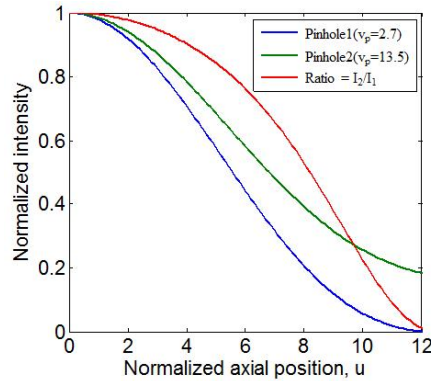

Fig. 2. Theoretical axial response curves of the intensity and intensity ratio in DDCFM. The intensity signals measured by each PMT differ because of different pinhole sizes. The blue and green line graphs show the axial response curves of the small ($v_p = 2.7$) and large ($v_p = 13.5$) pinholes, respectively. The ratio of the axial response curves is indicated by the red line. Since the relationship between the intensity ratio and the axial position is one-to-one, the intensity ratio directly indicates the axial position of the fluorescence source.

3. System setup

To demonstrate the feasibility of the proposed method, we built a DDCFM system, as shown in Fig. 3. The DDCFM has two detectors, each with a pinhole of a different diameter. A 488nm wavelength laser (35-LAL-030-220, Melles Griot, NM) was used as the light source. After it was collimated, the excitation beam passed the excitation filter (LL01-488-25, Semrock, NY). A dichroic mirror (Di02-R488, Semrock, NY) reflected the beam to a 2-D scanner comprising a galvanometer mirror (6240H, Cambridge technology, MA) and a resonant mirror (000-3015013, GSI Lumonics, MI). This scanner system was used to rapidly scan the x-y plane of the fluorescent sample. An imaging rate of 15.6 frames per second with 512 × 512 pixels was achieved using the resonant mirror with a resonant frequency of 8kHz. A relay lens expanded the beam diameter by three times and caused the beam to pass through the center of the objective while scanning the imaging field. The relay lens enabled the system to have a large field-of-view (FOV), up to 4000 × 4000 µm. An objective lens (378-801-6, Mitutoyo, Japan) focused the beam onto the fluorescent sample. The FWHM of the

axial response curve depends on the NA of the objective and the pinhole size. An objective lens with a relatively low effective NA of 0.045 was used for long axial measurements. Light emitted from the fluorescent sample traveled back through the objective, relay lens, x-y scanner, dichroic mirror, and emission filter (FF03-525/50-25, Semrock, NY).

The filtered beam was divided by a 50/50 beam splitter (BS010, Thorblas, NJ). The two beams were focused by two collecting lenses (NT47-641, Edmund, NJ) onto pinholes of different sizes. The diameter of the airy disk on the pinhole was used to determine the pinhole sizes [31]. The airy disk diameter was 42.7 μm at the detection plane. The small and large pinhole diameters were 30 μm and 150 μm, respectively. The fluorescent emission was measured by the two PMTs (H6779-20, Hamamatsu, Japan).
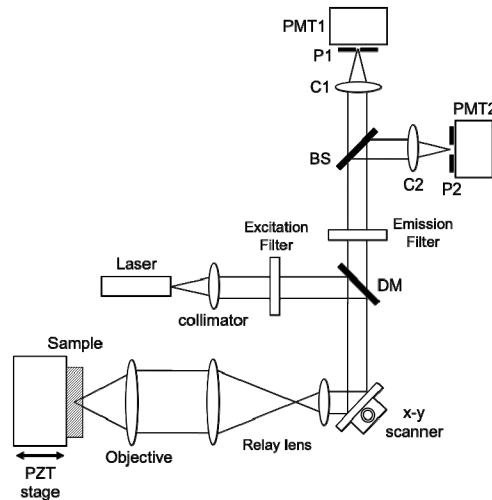

Fig. 3. Schematic of the experimental setup. The laser source was collimated then passed through an excitation filter. The beam was reflected by a dichroic mirror (DM) and scanned by an x-y scanner. A relay lens optical system directed the beam to the center of a 0.045-NA objective, despite various beam angles. The sample was precisely moved in the axial direction by a PZT stage. Light emitted from the sample passed inversely through the optical components and then through a dichroic mirror (DM) and emission filter. A 50/50 beam splitter (BS) divided the beam path equally, and two collecting lenses (C1, C2) focused the beam onto the PMTs. The pinhole in front of PMT 1 was smaller than the pinhole in front of PMT 2. The pinhole diameters were 30 μm and 150 μm.

4. Experiment and results

We tested the performance of DDCFM by imaging various fluorescent beads and a fluorescent-stained sample. We measured the axial response curve of DDCFM. A fluorescent sample with sparsely distributed standard fluorescent beads was prepared by spreading 6 μm fluorescent beads (I-14785, Invitrogen, CA) on a glass slide. We used the piezoelectric (PZT) stage (MIPOS, piezosystem jena, MA) to move the fluorescent sample axially in 1 μm increments over a 300 μm range. The bead intensity was measured by two PMTs at each step.

Figure 4 shows the measured axial response curves of DDCFM. As the fluorescent beads moved away from the focal point, the bead intensity decreased for both the small and large pinholes. The normalized intensities measured with the small and large pinholes are indicated by the blue and green lines, respectively. The two axial response curves show that the intensity at the small pinhole decreased rapidly as the bead moved out of focus. On the other hand, the signal decrease was much slower for the large pinhole. The ratio of the two curves is shown by the red line, which illustrates the dependency of the axial position on the ratio of the two axial response curves. These curves were used as a standard to calculate the axial position of a fluorescent emitter from the intensity ratio without axial scanning.

Part of the intensity ratio curve (red line) ranging from 45 μm to 225 μm was fitted as quintic polynomial to form a calibration curve, since the ratio and height have a relatively linear relation. Thus, in this experiment, the axial measurement range was 180 μm.
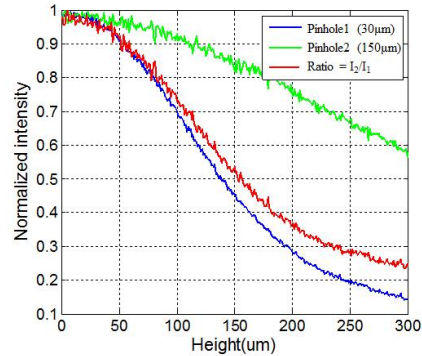

Fig. 4. Axial response curves. At each height, intensity was measured with 30 μm (blue) and 150 μm (green) pinholes. The intensity ratio of pinholes 1 and 2 is shown in red. Using the intensity ratio curve, the axial position of a fluorescent particle can be measured.

To evaluate the performance of DDCFM, the height of a fluorescent bead was measured when the bead moved axially from the focal plane. The fluorescent sample was 6 μm fluorescent beads spread sparsely on a glass slide. The sample was attached to the PZT stage to change the sample height. Two PMTs detected the fluorescence intensities as the beads moved. The ratio of two PMT signals was calculated, and the bead height was calculated from the height measurement curve.

Figure 5 shows the axial movement of a bead. Figures 5(a) and 5(b) show linear and step sample movements, respectively. The solid blue lines show the stage movement, and green spots show the bead height measured by DDCFM. To accurately evaluate the axial position, the standard deviation (SD) of the difference between the stage height and measured height was calculated. The SD was 7.42 μm for linear movement and 4.98 μm for step movement.
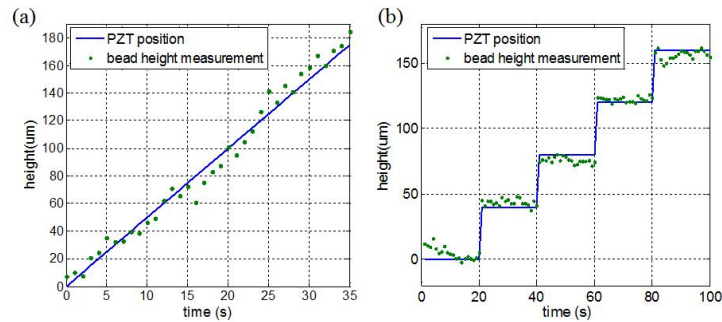

Fig. 5. Height variation measurement. The solid line represents the real PZT movement, and closed circles are the measured axial positions of a bead. (a) Linear bead movement. (b) Step bead movement.
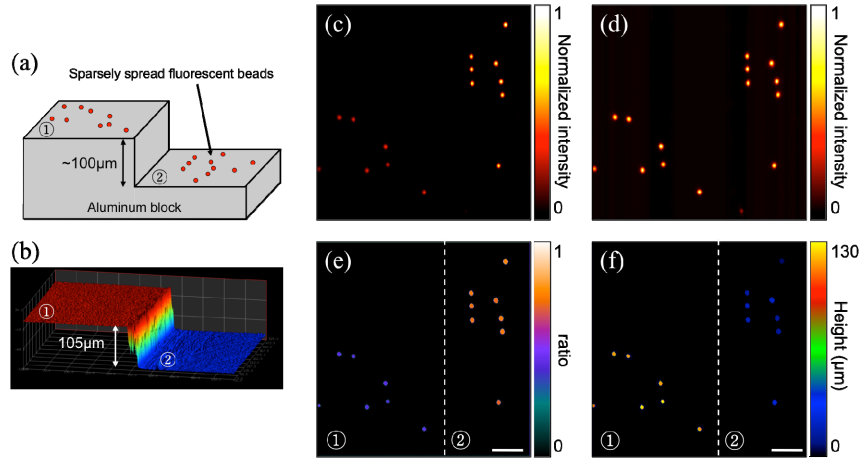
Fig. 6. DDCFM measurement of a fluorescent sample comprising two levels of 6 μm fluorescent beads separated by 105 μm. (a) Schematic of the sample. (b) 3-D surface image of a step sample taken with confocal reflectance microscopy. (c,d) Fluorescence intensity images of beads measured by the small and large pinholes, respectively. (e) Normalized ratio of intensity image. (f) Corresponding height image of beads. The beads on levels ① and ② are separated by 105.6 μm on average. Scale bars: 100 μm.

To demonstrate the 3-D imaging capabilities of DDCFM, a 3-D sample was prepared then imaged. The 3-D sample was made by placing fluorescent beads at two different heights. An aluminum block was machined into a step shape, as shown in Fig. 6(a). The difference in level height was 105 μm (Fig. 6(b)), as determined by commercial 3-D confocal microscopy (NS-I3500, Nanoscopesystems, Korea). Fluorescent beads were sparsely spread on the block, so that beads on level ① were 105 μm higher than beads on level ②.

For DDCFM, the focus was scanned over a single 700 × 700 μm lateral plane. Height information was collected in a single 2-D DDCFM scan. Figures 6(c) and 6(d) show the 2-D images from the small and large pinhole, respectively. The resulting normalized ratio of intensity, shown in Fig. 6(e), shows beads distributed on the two steps in the x-y plane. Since the focal plane was close to level ②, the ratio for beads on level ② was larger than that for beads on level ①. The ratios of beads on each level were clearly different, while the beads on the same level had similar ratios. From the intensity ratio image, the height of each emitter was reconstructed over a wide transverse x-y field and is represented by color bar in Fig. 6(f). Mean bead heights on levels ① and ② were 122.3 μm and 16.7 μm, respectively. The mean distance between the two levels was calculated to be 105.6 μm, which shows that DDCFM accurately measures fluorescent sample heights. The SD of the height measurement, which represents the accuracy of DDCFM, was 6.5 μm on the left and 5.1 μm on the right.

We tested whether DDCFM performs well with samples of varying brightness. As shown in Fig. 7(a), the sample comprised two kinds of fluorescent beads with different quantum yields (I-14785 (100%) and (0.3%), Invitrogen, CA) on a glass slide. Although all beads were on the same flat surface, the bead intensities differed due to different quantum yields (Figs. 7(b) and 7(c)). The bead heights could not be calculated by intensity measured with only one PMT because of varying intensities. The intensity ratio, however, was not influenced by quantum yield. As shown in Fig. 7(d), the intensity ratios were uniform regardless of quantum yield. Based on these ratios, Fig. 7(e) shows the height map of beads that were uniformly distributed with a SD of 8.86 μm. These results show that DDCFM is able to precisely measure the axial positions of fluorescent emitters with various quantum yields.
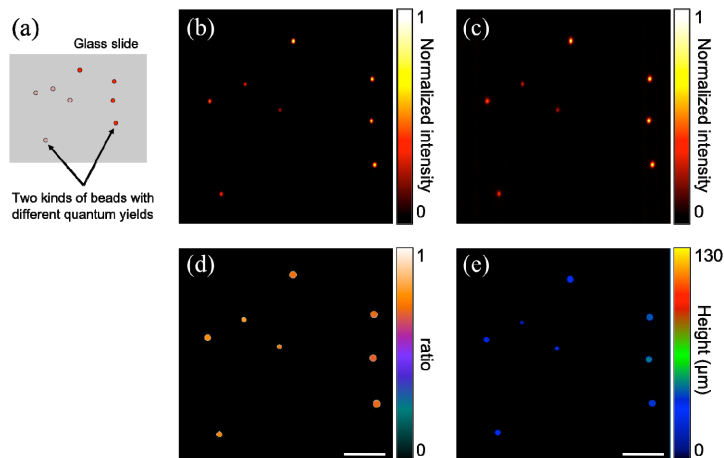
Fig. 7. DDCFM measurement of a fluorescent sample comprising 6 μm fluorescent beads with two different quantum yields on a glass slide. (a) Schematic of a sample. (b,c) Fluorescence intensity images of beads measured by the small and large pinholes, respectively. (d) Normalized intensity ratio image. (e) Corresponding height image. Despite varying quantum yields, bead heights were measured uniformly. Scale bars: 100 μm.

To demonstrate the potential of DDCFM to image 3-D structures, 3-D image of a fluorescent sample was obtained with a single 512 × 512 pixel raster scan without depth scanning. The sample was knitted nylon fabric stained with fluorescein (fluorescein sodium salt, Sigma-Aldrich, MO). Figure 8 shows fluorescent images of the nylon fabric structure. Figures. 8(a) and 8(b) are normalized intensity images of the nylon fabric in a 4000 × 4000 × 180 μm field of view taken with small and large pinhole, respectively. Large field of view and large depth range was obtained using an objective lens with low NA (NA = 0.045). A median filter and an averaging filter with a size of 3 × 3 pixels were applied to the DDCFM images to reduce the noise. Pixels having intensity below a certain threshold (0.05 × max intensity) were removed from calculation. After image pre-processing, intensity ratio was calculated then converted to height information. The corresponding 3-D reconstruction, shown in Fig. 8(c), was colored according to sample height. Different height of nylon fibers can be seen in the color-coded height map.

Also, we acquired a stack of 2-D images of the same sample with a confocal microscopy mode to directly compare the DDCFM with conventional confocal microscopy. We acquired a total of 181 sections with a confocal microscopy mode using the small pinhole, while moving the sample axially by 1 μm at each step. In order to reduce the width of axial response curve, we used different objective lens with higher NA (NA = 0.16) (UPLSAPO 4x, Olympus, Japan). Figure 8(d) shows two representative 2-D confocal images acquired with a confocal microscopy mode. Due to higher NA and larger magnification, the field of view was reduced by half. 2-D confocal images with different depth clearly show different fabric structure. Height map was calculated from the stack of confocal images by finding the axial (z) position whose intensity was maximized at a given transverse (xy) position. Color-coded height map is shown in Fig. 8(e). We acquired DDCFM image with a reduced field of view using low NA objective lens (NA = 0.045) to directly compare the DDCFM with confocal microscopy. Height map acquired by DDCFM without axial scanning is shown in Fig. 8(f). DDCFM (Fig. 8(f)) shows similar 3-D structure to confocal microscopy (Fig. 8(e)). Axial (xz) intensity images of the sample, reconstructed from 2-D stack of confocal microscopy (Fig. 8(g)) and height profile of DDCFM (Fig. 8(h)) show similar pattern.
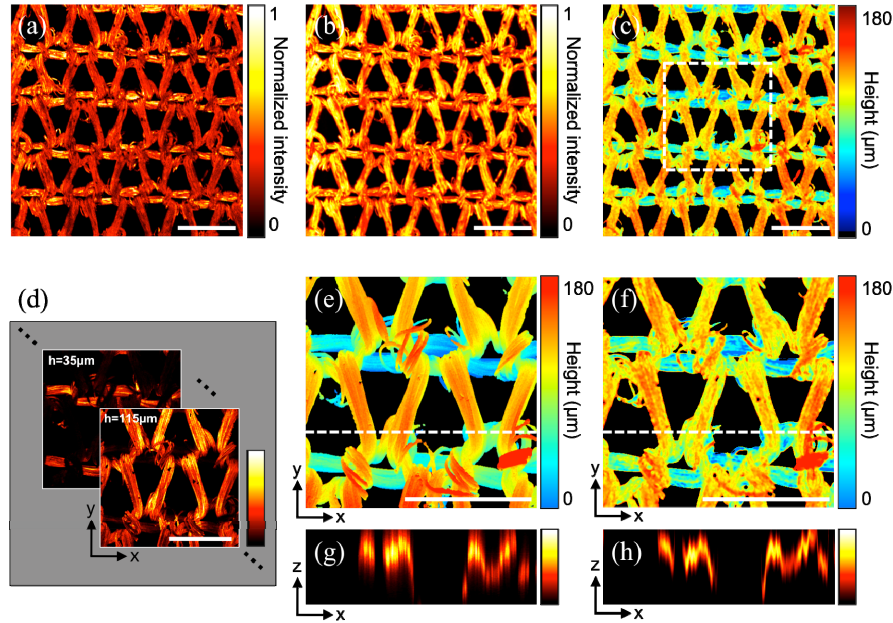
Fig. 8. DDCFM images of the 3-D structure of knitted nylon fabric. (a,b) Fluorescence intensity images of fabric with small and large pinhole, respectively. (c) Corresponding height image of nylon fabric. (d) Representative images of 2D stack of confocal microscope mode. (e) Reconstructed height map of nylon fabric by confocal microscope mode with high NA objective (NA = 0.16). (f) Optically zoomed height map of ROI (white dashed square) in (c) by DDCFM with low NA objective (NA = 0.045). (g) xz cross-section (1800 × 180 μm) of white dashed line in (e). (h) xz cross-section (1800 × 180 μm) of white dashed line in (f) with SD of 10 μm. Color bars in (d),(g), and (h) show normalized intensity. Scale bars, 1mm.

5. Conclusion

In conclusion, we have presented the dual detection confocal fluorescence microscopy method to detect the axial position of fluorescent particles with a single shot. Two point detectors with different pinhole sizes receive simultaneous fluorescent signals, which depend on the pinhole size and axial position of the fluorescent particle. The intensity ratio can be used to precisely measure the axial position where the fluorescence is emitted. DDCFM can provide depth information of a fluorescent sample at high speed because no mechanical depth scanning is needed. Since this method measures a depth location of fluorophore, not a full depth profile, if there is more than one fluorophore along the axial (z) direction at a transverse (xy) position, the depth measurement might be inaccurate. In this case, we anticipate that DDCFM measures the top position of the multiple fluorophores, since the closest fluorescent particle contributes most to the intensity ratio. Thus, the presented method works well for sparse fluorescent samples and surface profile, while it might have some errors for measuring dense samples with multilayer structure. Our results show that DDCFM is capable of visualizing fluorescent 3-D object with a reasonably complex structure as well as single fluorescent bead. Since DDCFM does not use repeated 2-D scans to create a 3-D reconstruction, photobleaching and phototoxicity can be greatly reduced compared to conventional laser scanning confocal fluorescence microscopy. Also, DDCFM has great potential to be miniaturized for a compact, endoscopic, 3-D fluorescence imaging probe.

Acknowledgments